Effect of Dielectric Permittivity Distribution in Invaded Zone on Induction Log Data

Igor Yeltsov[1,2,3], Timofey Eltsov[1,2,3], Aleksandr Makarov[4], and Marina Nikitenko[1,4]

[1] Institute of Petroleum Geology and Geophysics of SB RAS, Novosibirsk, Russia
[2] Novosibirsk State University, Novosibirsk, Russia
[3] Novosibirsk State Technical University, Novosibirsk, Russia
[4] Baker Hughes, Novosibirsk, Russia
yeltsovin@ipgg.sbras.ru

Abstract. The objective of this study is to demonstrate the effect of changes in dielectric permittivity on induction logging data during invasion evolution. As an investigation method we use invasion simulation and electromagnetic (EM) modeling of induction tool responses. In this study we simulate signals of EM tools to analyze the influence of different types of dielectric permittivity distribution and to estimate the influence of dielectric permittivity on induction logging signals. Analysis of the computed induction tool signals shows that dielectric permittivity influence on magnetic field attenuation is higher than on magnetic field phase difference. Induction measurements (transmitter frequency > 1 MHz) are significantly influenced by dielectric permittivity distribution in the invaded zone. The highest influence of dielectric permittivity on induction logging signals is observed in the case of low formation water saturation and high resistivity of drilling mud.

Keywords: Mud invasion, near wellbore dielectric permittivity distribution, near wellbore dielectric resistivity distribution, invaded zone, induction logging tool, electromagnetic modeling

Introduction

The mud invasion process causes formation fluid displacement that results in changes of resistivity and dielectric permittivity distribution (electro-physical properties) in the near wellbore zone. For conducting a correct interpretation of electromagnetic logging data, it is necessary to take into account varying resistivity and dielectric permittivity distribution in the invaded area, as far as these parameters affect induction logging measurements.

Near wellbore water saturation and salinity distributions can be described by numerical modeling of the mud filtrate penetration into the formation. The Buckley-Leverett equations for two-phase flow in porous media are used to carry out mud invasion simulation. These distributions are utilized to calculate resistivity and dielectric permittivity profiles using Archies equation and the complex refractive index method (CRIM) respectively. To estimate the influence of

resistivity and dielectric permittivity on induction logging signals we use electromagnetic (EM) modeling. Signals of induction logging tools are computed using an axisymmetric cylindrically layered earth model.

1 Dielectric permittivity mixing laws used for an oil and water saturated formation

There are many different mixing laws described in literature, all of them having empirical type. One of the most well-known equations is the Bruggeman mixing law:

$$\left(\frac{\epsilon_{\mathrm{m}} - \epsilon_{\mathrm{eff}}}{\epsilon_{\mathrm{m}} - \epsilon_{\mathrm{w}}}\right)\left(\frac{\epsilon_{\mathrm{w}}}{\epsilon_{\mathrm{eff}}}\right)^{\frac{1}{3}} = \phi \,, \tag{1}$$

where ϵ_{m} — complex permittivity of the matrix grains, ϵ_{w} — complex permittivity of the saturating brine, ϵ_{eff} — effective permittivity of the rock, ϕ — volume fraction of the saturating brine.

The main merit of the Bruggeman mixing law is taking into account interaction between fractions of the rock. There are only two different types of fraction: saturating brine in the separated spheres inside the matrix. There is an option to use the Bruggeman mixing law for a three component system (water, oil and matrix) proposed by [13]. In the proposed geometry each matrix grain is coated layer-by-layer with oil and water, but that could be applied only to oil-wet rocks.

There is an algorithm of dielectric permittivity mixing, proposed by Shelukhin and Terentev [14]. Actually it is the most complex and modern way of modeling the dielectric permittivity of a multicomponent system, but it is too complicated for usage and it is not suitable for our purposes, because it was not verified via laboratory experiment.

Further come the most extensively applicable mixing laws [13] used for multicomponent systems. The j-scaled mixing law is:

$$\epsilon_{\mathrm{eff}}^{\frac{1}{j}} = \sum_{n=1}^{N} \phi_n \epsilon_n^{\frac{1}{j}} \,, \tag{2}$$

where n — number of a single component, ϵ_n — dielectric permittivity of a sample component, ϕ_n — fraction of a sample component, j — empirical constant estimated from experimental measurements, N — a number of components.

The volumetric mixing law is defined as:

$$\epsilon_{\mathrm{eff}} = \sum_{n=1}^{N} \phi_n \epsilon_n \,. \tag{3}$$

The Birchak mixing law is:

$$\epsilon_{\mathrm{eff}}^{\frac{1}{2}} = \sum_{n=1}^{N} \phi_n \epsilon_n^{\frac{1}{2}} \,. \tag{4}$$

The complex refractive index method (CRIM) or Birchaks mixing law proposed by Birchak and others [2] was checked by [11] and [13], who experimentally proofed that the CRIM formula is the most reliable in the case of a three-component system (measurements of electro physical parameters in a laboratory for a wide frequency range). The CRIM model is based on the optical path length of a single electromagnetic ray. It is equivalent to a volumetric average of the complex refractive index, and it assumes that total transit time of a propagating pulse is equal to the sum of transit times of the constituents [13].

The Looyenga-Landau-Lifshiz mixing model:

$$\epsilon_{\text{eff}}^{\frac{1}{3}} = \sum_{n=1}^{N} \phi_n \epsilon_n^{\frac{1}{3}} \ . \tag{5}$$

The Lichtenecker's mixing law is as follows:

$$\ln \epsilon_{\text{eff}} = \sum_{n=1}^{N} \phi_n \ln \epsilon_n \ . \tag{6}$$

The CRIM formula was chosen because it was verified by well-known specialists and it is applicable for multicomponent systems.

For modeling we chose typical resistivities of water-based drilling mud. Formation water saturations were selected in such a way as to cover both water and oil saturated reservoirs. Dielectric permittivity of mineralized water was set according to Fig. 1 [8]. Water saturations were selected to cover both water and oil saturated reservoirs. Analysis of current publications allowed us to select typical examples of petrophysical properties of oil and water saturated sandstones.

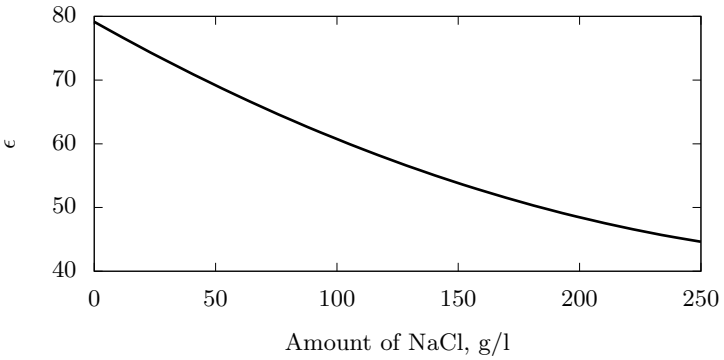

Fig. 1. Dependence of dielectric permittivity of NaCl solution on mineralization at temperature of +20 °C [8]

2 Dielectric Permittivity Distribution Modelling

Fig. 2 shows the formation earth model utilized for invasion and electromagnetic modeling, which is a radial axisymmetric layered medium. The layers are: borehole, formation and a number of layers between them characterizing the distribution of dielectric permittivity ($\epsilon_{\text{iz}}(r)$) and resistivity ($\rho_{\text{iz}}(r)$) in the invaded zone. ϵ_{f} and ρ_{f} are correspondingly dielectric permittivity and resistivity of undisturbed formation. The modeling is divided into two parts. The first part is invasion zone modeling that provides water saturation and salinity distributions in near wellbore area.

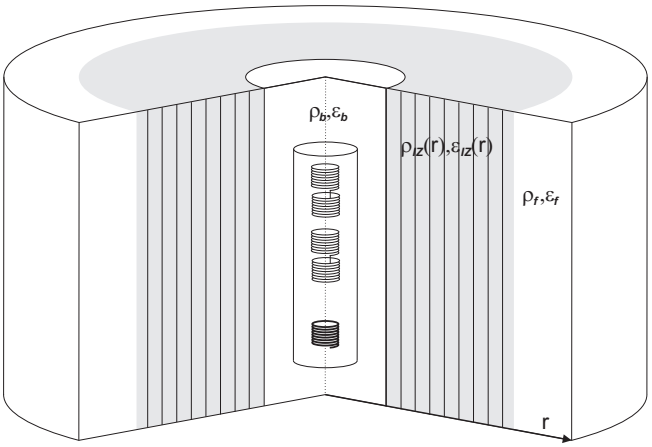

Fig. 2. Geoelectric model of medium. Cylindrically layered formation, characterized by n radial layers

2.1 Invasion Zone Simulation

Reservoir drilling is accompanied by mud invasion into a permeable formation. Mud solids plug the near-wellbore area and form a low-permeability mudcake at the borehole wall. The mudcake reduces the rate of mud filtrate invasion and slows the invaded zone extension. The formation properties, such as resistivity, density and others, change in the near-wellbore zone, depending on mud filtrate penetration and displacement of formation fluids. Mud invasion structure can be estimated via inversion of electromagnetic log data measurements [5]. In this study, the aim of invasion modeling is to compute water saturation and salinity distributions in the invaded zone.

Water-based mud filtration is simulated using mud reports, drilling regime data and available a-priori information, such as formation and mudcake properties [15, 3, 7]. We consider the Buckley-Leverett model without capillary forces

to describe the invasion of water-based mud into a reservoir saturated by oil and water [9, 4]. The transport equations for the 1D radial axi-symmetric case are the following:

$$\frac{\partial}{\partial t}\left(r\phi_{\mathrm{f}}S_{\mathrm{w}}\right)=\frac{\partial}{\partial r}\left(rk_0\frac{k_{\mathrm{w}}}{\mu_{\mathrm{w}}}\frac{\partial p}{\partial r}\right),\qquad R_{\mathrm{wb}}<r<L\,, \tag{7}$$

$$\frac{\partial}{\partial t}\left(r\phi_{\mathrm{f}}S_{\mathrm{oil}}\right)=\frac{\partial}{\partial r}\left(rk_0\frac{k_{\mathrm{oil}}}{\mu_{\mathrm{oil}}}\frac{\partial p}{\partial r}\right),\qquad R_{\mathrm{wb}}<r<L\,, \tag{8}$$

$$\phi_{\mathrm{f}}=\phi_0+\lambda p\,, \tag{9}$$

$$S_{\mathrm{oil}}+S_{\mathrm{w}}=1\,, \tag{10}$$

where r is the distance from the center of the wellbore to the remote part of the formation. The region of modeling is $R_{\mathrm{wb}}<r<L$, where R_{wb} is the wellbore radius and L is the boundary of the modeling area. L is the distance at which pressure in the near-wellbore zone equals the formation pressure, $L\gg R_{\mathrm{wb}}$; at distances greater than L, pressure does not change; t is the modeling time that varies from 0 (the beginning of reservoir drilling) up to T_{d} (time since the reservoir drilling); p is the pressure difference between the well pressure and formation pressure; $S=S_{\mathrm{w}}$, S_{oil} are the saturations of water and oil fractions, respectively; ϕ_{f} is the formation porosity; ϕ_0 is the porosity of the undisturbed formation; λ is the compressibility of the formation; $k_{\mathrm{w}}(S_{\mathrm{w}})=S_{\mathrm{w}}^{n_{\mathrm{w}}}$, $k_{\mathrm{oil}}(S_{\mathrm{oil}})=S_{\mathrm{oil}}^{n_{\mathrm{oil}}}$ are the functions of phase permeabilities; n_{w}, n_{oil} are the empirical exponents found from petrophysical analysis (Corey-Brooks constants); μ_{w}, μ_{oil} are the viscosities of water and oil, respectively; k_0 is the absolute permeability of the formation.

The boundary and initial conditions are added to the equations (7) and (8), and mud filtration through mudcake is determined by the expression:

$$p|_L=0,\ p|_{t=0}=0,\ Q(t)=R_{\mathrm{wb}}\frac{\left(P_{\mathrm{wb}}-p|_{r=R_{\mathrm{wb}}}\right)}{\left(b_0^{-1}+d\mu_{\mathrm{w}}/k_{\mathrm{c}}\right)},\ S|_{t=0}=S_{\mathrm{f}},\ S_{R_{\mathrm{wb}}-d}=1\,, \tag{11}$$

b_0^{-1} is the filtration drag of the plugging zone; d is the mudcake thickness; k_{c} is the mudcake permeability; P_{wb} is the pressure drop from the wellbore to the formation; Q is the mud filtrate flow rate and S_{f} is the initial formation water saturation. The mudcake thickness, permeability and porosity are assumed to be constant, which significantly simplifies the filtration model. To solve the system of the equations (7)–(11) the numerical solution was implemented.

Combining the equations (7) and (8), and taking into account the equations (9)–(11), we obtain the following piezo-conductivity equation [1]:

$$\lambda\cdot r\cdot\frac{\partial p}{\partial t}=\frac{\partial}{\partial r}\left[\lambda\cdot k_0\cdot\left(\frac{k_{\mathrm{w}}}{\mu_{\mathrm{w}}}+\frac{k_{\mathrm{oil}}}{\mu_{\mathrm{oil}}}\right)\frac{\partial p}{\partial r}\right],\qquad R_{\mathrm{wb}}<r<L\,. \tag{12}$$

Salt transport during invasion occurs because of formation fluid and mud filtrate mixing. The water phase transport is caused by pressure overbalance.

Salinity transport modeling is described using the following transport equation and boundary conditions:

$$\frac{\partial}{\partial t}\left(r\phi_{\mathrm{f}}SC\right) = \frac{\partial}{\partial r}\left(rk_{\mathrm{w}}\frac{\partial p}{\partial r}C\right) , \tag{13}$$

$$C|_{t=0} = 1, \qquad C_{R_{\mathrm{wb}}} = 0 , \tag{14}$$

where C is the relative salinity that is equal to C_{wb} in mud filtrate and to C_{f} in formation brine. To evaluate the true salinity profile, the relative salinity distribution should be normalized by the true salinity values. The finite-difference scheme is developed and realized for the solution of the system of equations (7) - (14). Firstly, the pressure overbalance distribution is computed via implicit finite-difference method for equation (12). Secondly, for the computation of water saturation and salinity distribution the explicit finite-difference method is used, after that, the computation goes to the next time step, and the scheme is realized again until the simulation time T_d. The parameters used for invasion simulation are shown in the Table 1.

Table 1. Invasion simulation parameters

Parameter		Value
Formation permeability, D	k_0	0.1
Initial formation water saturation, fraction	S_{f}	0.2, 0.4, 0.6
Formation compressibility, atm^{-1}	λ	0
Formation porosity, p.u.	ϕ_{f}	25
Borehole radius, m	R_{wb}	0.108
Pressure overbalance, atm	P_{wb}	10
Time since reservoir drilling, day	T_{d}	0.2
Mudcake permiability, D	k_{c}	0.00001
Mudcake thickness, m	d	0.001
Corey-Brooks constant for oil phase permeability, unitless	n_{oil}	2.5
Corey-Brooks constant for water phase permeability, unitless	n_{w}	3.0
Oil viscosity, cP	μ_{oil}	10.0
Water viscosity, cP	μ_{w}	1.0

2.2 Calculation of Resistivity and Dielectric Permittivity Profiles

These distributions are used to calculate the resistivity and dielectric permittivity profiles via Archie's equation and the CRIM model. The following Archie's equation is used:

$$\rho_{\mathrm{iz}}(r) = \rho_{\mathrm{w}}(r)\phi_{\mathrm{f}}^{-m}S_{\mathrm{w}}^{-n}(r) , \tag{15}$$

here $n = 2$, $m = 1.5$ - Archie's exponents, $\rho_{\text{iz}}(r)$ — invasion zone resistivity; $\rho_{\text{w}}(r)$ — water fraction resistivity; ϕ_{f} — formation porosity; $S_{\text{w}}(r)$ — water saturation distribution.

Calculation of dielectric permittivity distribution using the CRIM model comprises the following steps. Firstly, it is necessary to calculate the volume fractions of each constituent. Knowing water saturation distribution $\phi_{\text{w}}(r)$ in the near borehole zone it is easily to calculate the volume fractions of matrix $\phi_{\text{m}}(r)$ and oil $\phi_{\text{oil}}(r)$ in the whole space of interest.

$$\phi_{\text{w}}(r) = \phi_{\text{f}} S_{\text{f}}(r) \,, \tag{16}$$

$$\phi_{\text{oil}}(r) = \phi_{\text{f}} - \phi_{\text{w}}(r) \,, \tag{17}$$

$$\phi_{\text{m}}(r) = 1 - \phi_{\text{f}} \,. \tag{18}$$

Secondly, after volume fraction calculation, dielectric permittivity distribution is calculated in each point in the near borehole zone using the CRIM formula:

$$\epsilon_{\text{eff}}(r) = \left(\phi_{\text{m}} \epsilon_{\text{m}}^{\frac{1}{2}} + \phi_{\text{w}}(r) \epsilon_{\text{w}}^{\frac{1}{2}} + \phi_{\text{oil}}(r) \epsilon_{\text{oil}}^{\frac{1}{2}}\right)^2 \,, \tag{19}$$

where ϵ_{w} — dielectric permittivity of water fraction, ϵ_{oil} — dielectric permittivity of oil fraction, ϵ_{m} — dielectric permittivity of rock matrix.

3 Discussion

It is necessary to consider the difference between the radial profiles of electro physical parameters for different geological conditions. Pictures Fig. 3–5 show the distribution of electro-physical parameters of sandstones.

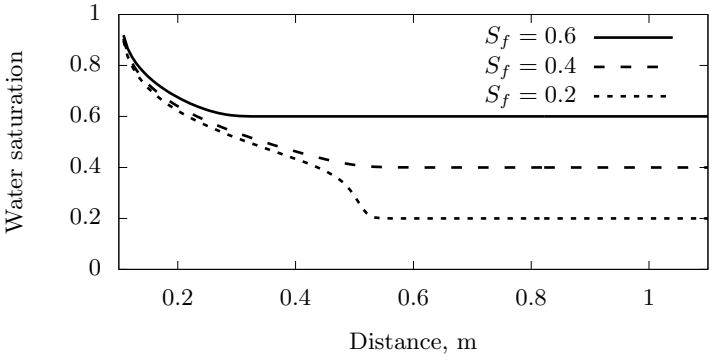

Fig. 3. Water saturation profile. Sandstone, porosity 25 p.u. Different water saturation of collector

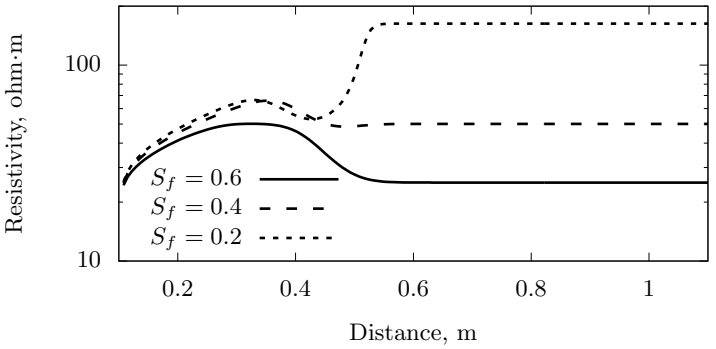

Fig. 4. Resistivity distribution. Sandstone, porosity 25 p.u. Different conductivities of brine

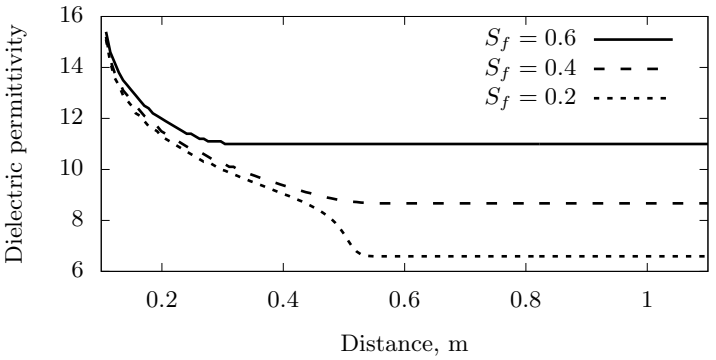

Fig. 5. Dielectric permittivity profile. Sandstone, porosity 25 p.u. Different water saturation of collector

Fig. 3 shows the dielectric permittivity distribution for sandstone, porosity 25 for different initial formation water saturations ($S_f = 0.2, 0.4, 0.6$).

The shape of water saturation profile (Fig. 3) looks like corresponding dielectric permittivity profile (Fig. 5). The reason of this phenomenon is due to the CRIM formula usage. The value of dielectric permittivity falls down from 15 to 6.7 (Fig. 5). The most significant change of dielectric permittivity along the invaded zone is for the lowest water saturation.

4 Signal Modeling

We simulate a vertical magnetic field component (H_z). The transmitter is assumed to be a vertical magnetic dipole. To simulate induction log synthetic responses, we use forward modeling software for the case of 1D coaxial cylindrical geometry.

Modeling is performed using the parameters of LWD resistivity tool. This LWD resistivity tool measures formation resistivity in real-time for indication of oil and gas saturated reservoirs [10]. It consists of three-coiled induction short-spaced (23 in.) and long-spaced (35 in.) probes, and operates on two frequencies: 400 kHz and 2 MHz. The measured signals are the magnetic field attenuation and magnetic field phase difference (between two receiver coils). Usually these signals are converted into apparent resistivities for further interpretation.

Also we simulate responses of the induction logging tool described in a patent application published by Nikitenko M.N. in 2009 [12]. In our paper this tool is called "Induction tool". Its frequency range is 1.75–24.5 MHz, with spacings varying from 0.18 m to 1 m. The three-coil array consists of a transmitter, a main receiver and a bucking coil. The moments are chosen in such a way as to compensate direct field. Seven different three-coil probes are considered. The parameters of the tools under consideration the distances between the coils and operating frequencies are shown in Table 2.

5 Influence of Dielectric Permittivity Distribution on Induction Logging Signals

The resistivity and dielectric permittivity profiles shown in Fig. 3–5 were selected as input earth models for the EM modeling of the induction log synthetic responses. Signals were modeled taking into account dielectric permittivity distribution and compared with signals modeled without dielectric permittivity distribution.

Influence of dielectric permittivity distribution on the LWD resistivity tool and high-frequency induction probes is noticeable. Before comparison of the signals it is necessary to estimate their level. The common value of the noise level is 0.01 dB. The common value of noise for the phase shift signal is 0.1 degrees. The signal was considered to be high if it was two times bigger than

Table 2. Induction tool and LWD resistivity tool modeling parameters

3 coil tool number	Lengths, m	Frequencies, MHz
	Induction tool	
1	0.18, 0.25	12.25, 24.50
2	0.22, 0.32	10.50, 21.00
3	0.28, 0.40	8.75, 17.50
4	0.35, 0.50	7.00, 14.00
5	0.45, 0.64	5.25, 10.50
6	0.56, 0.80	3.50, 7.00
7	0.70, 1.00	1.75, 3.50
	LWD resistivity tool	
1	0.47, 0.67	0.4
2	0.47, 0.67	2
3	0.80, 1.0	0.4
4	0.80, 1.0	2

the noise. The deviation between the signals is shown in errors. The error is calculated using the formula:

$$\delta = \frac{|S_{eps} - S_0|}{\gamma} , \tag{20}$$

where γ is value of noise (0.1 degree for phase difference and 0.01 dB for attenuation). S_{eps} — signal in case of media with dielectric permittivity distribution, S_0 — signal in media without dielectric permittivity distribution.

For most of the sandstone models the LWD resistivity tool signals are high enough. The exception is the most resistive models.

Fig. 6–8 exemplify the induction tool signals. Fig. 11–13 shows an example of the signals of LWD resistivity tool. The influence of dielectric permittivity distribution on induction tool signals is shown on Fig. 9–15.

The difference between the signals is shown for sandstone, porosity 25 p.u., mud conductivity 1 S/m, brine conductivity 0.5 S/m. The tool numbers are numbers of the three-coil tools shown in Table 3. Fig. 9 and Fig. 10 corresponds to the induction tool. The difference between the signals for all the frequencies and the longest array (0.7 m and 1 m) is shown in Fig. 9. The difference between the signals for the highest frequency and all the arrays at the highest frequency of the induction tool is shown in Fig. 10. The longer the tool spacing and the higher the frequency, the greater the permittivity influence is. The influence of dielectric permittivity distribution on the LWD resistivity tool signals is shown in Fig. 14 and Fig. 15. When considering the LWD resistivity tool signals we may note that the influence of dielectric permittivity is less than the noise value.

The overall results are shown in Table 3, where the differences between the signals are calculated using the equation (20).

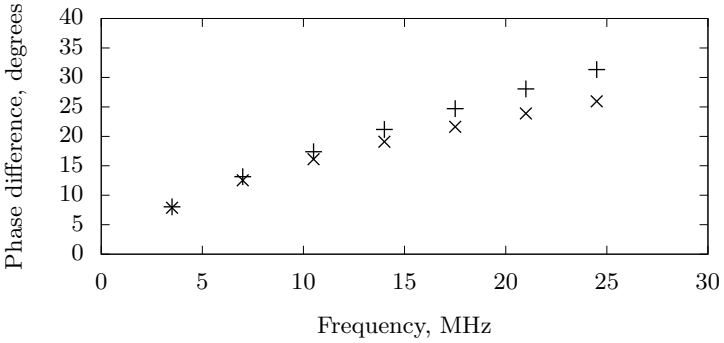

Fig. 6. The induction tool, longest array, all frequencies. Porosity 25 p.u., $S_{\mathrm{f}} = 0.6$, $C_{\mathrm{b}} = 0.5$ S/m, $C_{\mathrm{f}} = 1$ S/m. With (+) and without (×) dielectric permittivity distribution

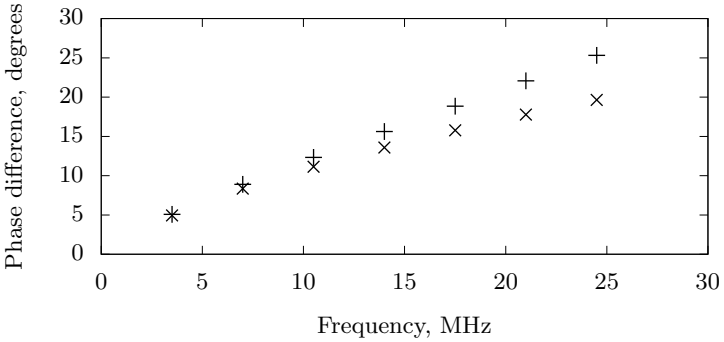

Fig. 7. The induction tool, longest array, all frequencies. Porosity 25 p.u., $S_{\mathrm{f}} = 0.4$, $C_{\mathrm{b}} = 0.5$ S/m, $C_{\mathrm{f}} = 0.1$ S/m. Symbols are the same as in Fig. 6

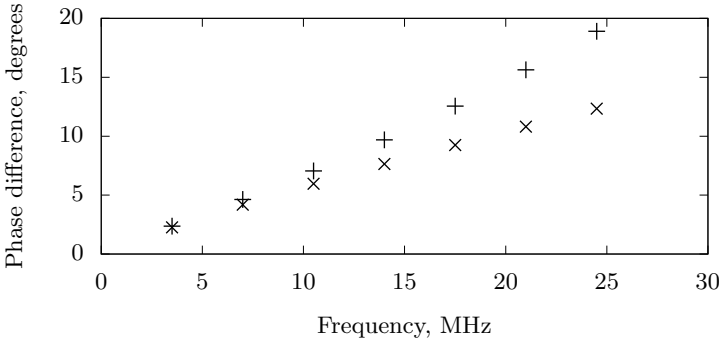

Fig. 8. The induction tool, longest array, all frequencies. Porosity 25 p.u., $S_{\mathrm{f}} = 0.2$, $C_{\mathrm{b}} = 0.5$ S/m, $C_{\mathrm{f}} = 1$ S/m. Symbols are the same as in Fig. 6

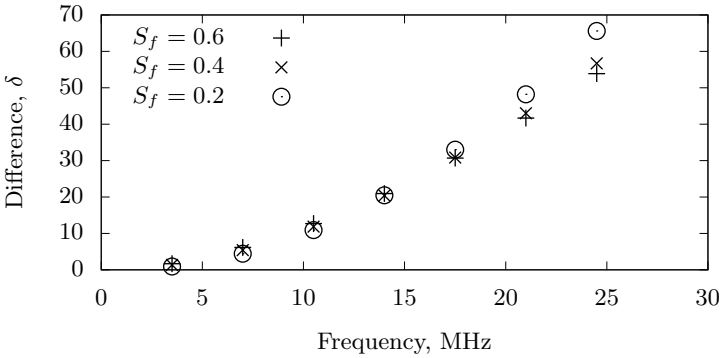

Fig. 9. The induction tool, longest array, all frequencies. Porosity 25 p.u., $C_{\text{b}} = 0.5$ S/m, $C_{\text{f}} = 1$ S/m

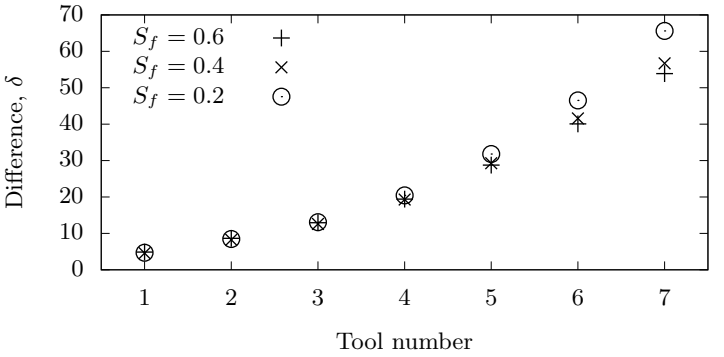

Fig. 10. The induction tool, highest frequency, all arrays. Porosity 25 p.u., $C_{\text{b}} = 0.5$ S/m, $C_{\text{f}} = 1$ S/m

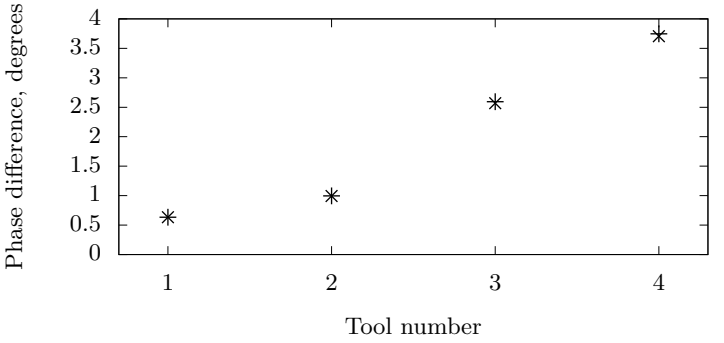

Fig. 11. LWD resistivity tool computed signals, longest array, all frequencies. Porosity 25 p.u., $S_{\text{f}} = 0.6$, $C_{\text{b}} = 0.5$ S/m, $C_{\text{f}} = 1$ S/m. Symbols are the same as in Fig. 6

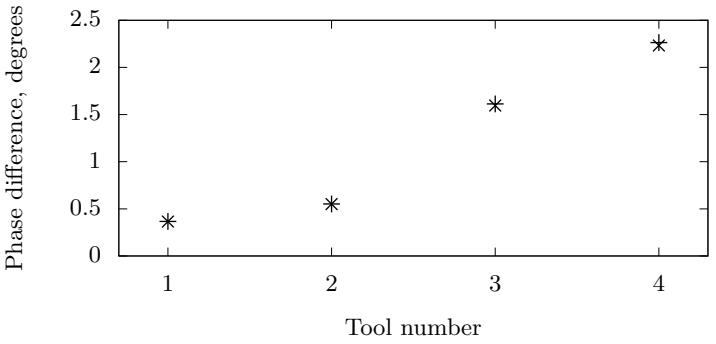

Fig. 12. LWD resistivity tool computed signals, longest array, all frequencies. Porosity 25 p.u., $S_{\mathrm{f}} = 0.4$, $C_{\mathrm{b}} = 0.5$ S/m, $C_{\mathrm{f}} = 1$ S/m. Symbols are the same as in Fig. 6

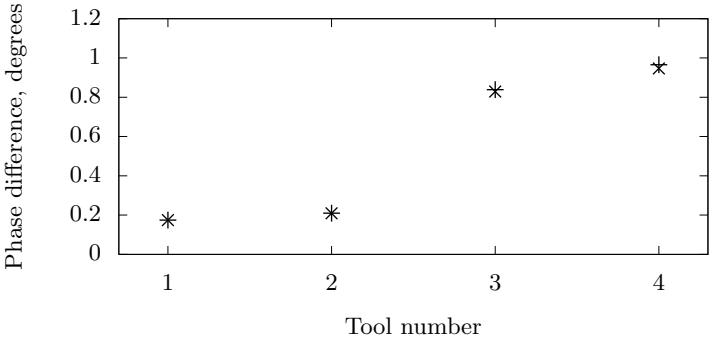

Fig. 13. LWD resistivity tool computed signals, longest array, all frequencies. Porosity 25 p.u., $S_{\mathrm{f}} = 0.2$, $C_{\mathrm{b}} = 0.5$ S/m, $C_{\mathrm{f}} = 1$ S/m. Symbols are the same as in Fig. 6

Fig. 14. LWD resistivity tool, difference of computed attenuations. Porosity 25 p.u., $C_{\mathrm{b}} = 0.5$ S/m, $C_{\mathrm{f}} = 1$ S/m

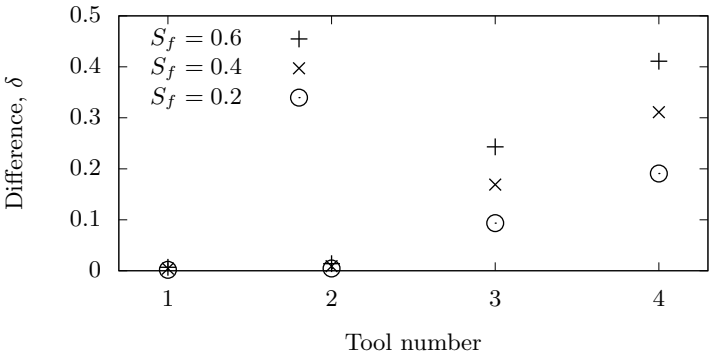

Fig. 15. LWD resistivity tool, phase discrepancy of computed phase differences. Porosity 25 p.u., $C_\mathrm{b} = 0.5$ S/m, $C_\mathrm{f} = 1$ S/m

Table 3. Difference between induction signals

	$S_\mathrm{f} = 0.2$	$S_\mathrm{f} = 0.4$	$S_\mathrm{f} = 0.6$
Induction tool			
Normal phase difference signal level, degrees	8–31.3	5–25	2–18
Phase signal difference, noise level	1–50	1–56	1–65
Normal attenuation signal level, dB	0.4–2.7	0.1–0.55	< 0.1
Attenuation signal difference, noise level	5–80	5–90	< 0.01
LWD resistivity tool			
Normal phase difference signal level, degrees	0.6–3.7	0.13–2.6	0.1–1
Phase signal difference, noise level	< 0.1	< 0.1	< 0.1
Normal attenuation signal level, dB	0.01–0.2	< 0.01	< 0.01
Attenuation signal difference, noise level	< 0.01	< 0.01	< 0.01

Summary

In this study, we propose a workflow of dielectric permittivity distribution computation in the near wellbore area, using invasion simulation and the complex refractive index method. The analysis of dielectric permittivity distribution computation shows that in case of low mud and brine conductivity ($C_\mathrm{b} = 0.5$ S/m, $C_\mathrm{f} = 1$ S/m) water saturation distribution is the main factor affecting dielectric permittivity distribution in the invaded zone. It is observed that dielectric permittivity distribution is almost insensitive to water salinity in case of low conductivity both mud and brine.

The numerical modeling of induction logging synthetic responses (LWD resistivity tool) shows that influence of dielectric permittivity distribution on the LWD resistivity tool phase difference of magnetic field is less than the value of the noise level (< 0.1 degree) for all the considered initial formation water saturations. Modeling of the induction tool signals shows that the influence of dielectric permittivity distribution on the phase difference of magnetic field is considerable in the case of high values of water saturation ($S_\mathrm{f} = 0.6$) and high values of fluid and mud and brine conductivity ($C_\mathrm{b} = 0.5$ S/m, $C_\mathrm{f} = 1$ S/m). The effect of dielectric permittivity distribution on the phase difference can be 2 times lower than that on the attenuation.

Dielectric permittivity distribution influence on the signals of the induction tool has been much higher than that on the LWD resistivity tool signals (up to 100 times of the noise values in the case of sandstone with low mineralization of brine and mud). It means that low frequency (less than 2 MHz) induction tools are more reliable for estimation of the resistivity profile through the LWD resistivity log data processing, as opposed to the induction tool measurements. We recommend using the joint inversion scheme based on invasion simulation and electromagnetic modeling.

Acknowledgments. This work was supported by RFBR grants 16-05-00830 and 16-35-00395.

References

1. Basniev, K. S., Kochina, I. N., Maksimov, V. M.: Subterranean hydrodynamics. Nedra (1993)
2. Birchak, R. J., Gardner, G. C., Hipp, E. J., Victor, J. M.: High dielectric constant microwave probes for sensing soil moisture. IEEE. 1974. 93–98
3. Chenevert, M. E., Dewan, J. T.: A model for filtration of water-base mud drilling: determination of mudcake parameters. Petrophysics, SPWLA, 42, 2001, no. 3, 237–250
4. Collins, R. E.: Flow of fluids through porous materials. Reinhold Publishing Corporation (1961)
5. Eltsov, I., Antonov, Y., Makarov, A., Kashevarov, A.: Invaded zone evolution reconstructed from logging data. Presented at the 81th Annual Meeting, SEG, 2011, Expanded abstracts, 509–513

6. Epov, M. I., et al.: Advanced Electromagnetic (EM) Tool. Novosibirsk: Baker Hughes (2006)
7. Epov, M. I., Yeltsov, I. N., Kashevarov, A. A., Sobolev, A. Yu., Ul'yanov, V. N.: Evolution of invaded zone inferred from electromagnetic logging and hydrodynamic modeling. Russian Geology and Geophysics, 2004, Vol. 45, No 8, pp. 985–995
8. Gavish, N., Promislow, K.: Dependence of the dielectric constant of electrolyte solutions on ionic concentration (2012)
9. Kashevarov, A. A., Yeltsov, I. N., Epov, M. I.: Hydrodynamic model for the evolution of an invaded zone in borehole drilling. Journal of Applied Mechanics and Technical Physics, 44, no. 6, 2003, 148–157
10. Meyer, W. H., et al.: A New Slimhole Multiple Propagation Resistivity Tool. Paper NN presented at the 1994 SPWLA Annual Logging Symposium, Tulsa, 19–22 June
11. Meyer, W. Hal.: Field measurements of resistivity dispersion using two frequency mwd propagation resistivity tools. Petrophysics 41, no. 6 (November–December 2000): 492–502
12. Nikitenko, M.N., Tabarovsky, L.A., Epov, M.I.: US Patent 7,567,869. Induction tool for detail evaluation of near borehole zone. July 28, 2009
13. Seleznev, N., Boyd, A., Habashy, T., Luthi, S. M.: Dielectric mixing laws for fully and partially saturated carbonate rocks. SPWLA 45th Annual Logging Symposium. June 6–9, 2004
14. Shelukhin, V. V., Terentev, S. A.: Frequency dispersion of dielectric permittivity and electric conductivity of rocks via two scale homogenization of the Maxwell equations. Progress in electromagnetic research 14 (2009): 175–202
15. Sherwood, J. D., Meeten, G. H.: The filtration of compressible mud filtercakes. Journal of Petroleum Science and Engineering, 1997, no 18, 73–81